

## CHAPTER 2

### LITERATURE REVIEW

#### 2.1 Theoretical issues of the dye sensitized solar cell operation

The dye-sensitized light-to-electron conversion process differs fundamentally from the one in the conventional solar cells. Figure 2.1 shows the energy band diagram of a p-n junction after thermal equilibration of charge carriers. The uncompensated charge caused by the diffusion of holes to the n region, and electrons to the p region, forms an electric field at the interface between the n and the p-type semiconductor (space charge layer; SPL), which is characterized by the built in potential  $V_{bi}$ . Absorption of photons with an energy higher than the band gap results in the generation of electron-hole pairs (excitons) which interact via columbic forces. Excitons recombine after a certain time under emission of photons or heat, unless they are separated by an electric field. Therefore only excitons created in the space charge layer or close to it will contribute to the photocurrent [5].

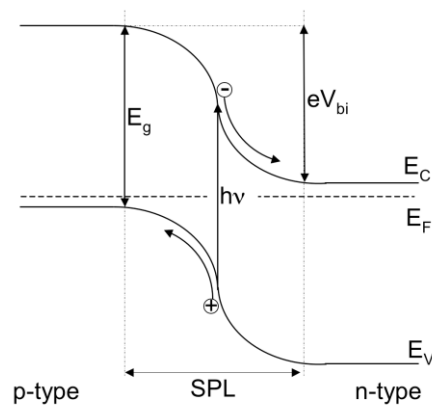


Figure 2.1 Energy band diagram of a conventional p-n junction solar cell under short circuit conditions [5].

Since the invention of the nanostructured dye-sensitized solar cell (DSSC), a lot of theoretical and experimental work has been carried out to explain the surprisingly efficient operation of these solar cells. The need for unique theoretical considerations of the photovoltaic effect in the DSSCs arises from the fundamental differences in the operation between the DSSCs and the traditional semiconductor p-n junction solar cells [5]:

- (1) Light adsorption and charge carrier transport are separated in dye-sensitized solar cell, whereas both processes are established by the semiconductor in the conventional cell.
- (2) An electric field is necessary for charge separation in the p-n junction cell. Nanoparticles in the dye-sensitized solar cell are too small to sustain a built-in field; accordingly charge transport occurs mainly via diffusion.
- (3) Inside a p-n junction minority and majority charge carriers coexist in the same bulk volume. This makes conventional solar cells sensitive to bulk recombination and demands the absence of any recombination centers such as trace impurities. Dye-sensitized solar cells are majority charge carrier devices in which the electron transport occurs in the metal oxide and the hole transport in the electrolyte. Recombination processes can therefore only occur in form of surface recombination at the interface.

### **2.1.1 Dye-sensitized solar cells**

Dye-sensitized solar cells have received great interest for their high efficiency, low-cost and varied and fine-tuned material choices. A typical DSSC consists of a dye-sensitized metal-oxides layer as the working electrode, an electrolyte containing a

redox couple ( $I_3^-/I^-$ ) and a Pt layer counter electrode. Many metal-oxides can be used as DSSC electrodes, such as  $TiO_2$ ,  $ZnO$ ,  $WO_3$ ,  $CdSe$ ,  $CdS$ ,  $Fe_2O_3$ ,  $SnO_2$  and  $Nb_2O_5$  and Titanium dioxide ( $TiO_2$ ) is the most popular electrode discussed for its band gap, surface structure, particle size, porosity and film thickness in improving DSSC performance and. However,  $TiO_2$  electron mobility is too low to further improve the conversion efficiency. Therefore, considerable research advances and studies on DSSCs have focused on the improvement of electron transport and reducing the recombination rate by the use of the different oxide semiconductor materials to replace  $TiO_2$ . There are many advantages with  $ZnO$  DSSC electrodes such as [12]:

- (1) Similar band gap as  $TiO_2$ .
- (2) Higher electron mobility.
- (3) Simpler tailoring.
- (4) Easier surface modification.

Furthermore due to its higher electronic mobility, it has been also chosen as an alternative of  $TiO_2$  which in DSSCs as working electrode.

### **2.1.2 Operating principle of the dye-sensitized solar cell**

The dye sensitized solar cell was developed by O'Reagan and Grätzel in 1991's originally. Following some innovations to achieve high conversion efficiency, it has recently reached over 11% [3]. In Figure 2.2, a schematic explanation of dye sensitized solar cells as the case of Eosin Y /  $ZnO$  system is shown. The combination of  $ZnO$  thin film, Eosin Y complex dye as sensitizer, and iodine containing electrolyte shows the highest efficiency so far. Pt is commonly used as counter electrode [13].

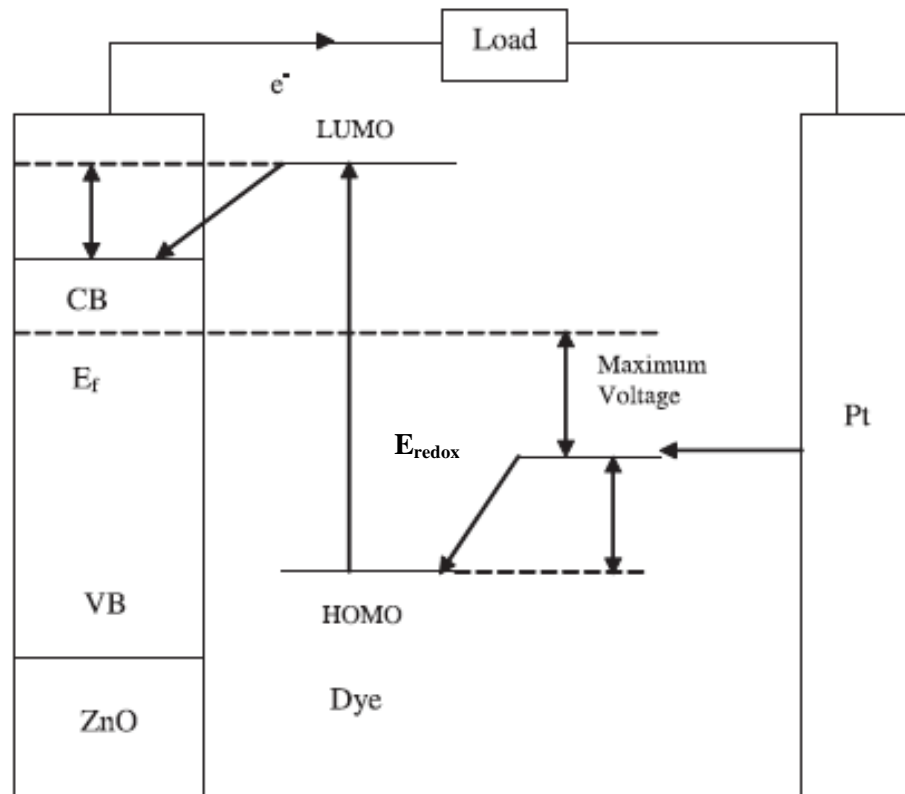


Figure 2.2 Schematic energy diagrams for a ZnO dye-sensitized solar cell [13].

Figure 2.2 The cells operate as following; first, the dye adsorbed on the surface of metal oxide semiconductor absorbs the photon, an electron is excited to the LUMO (lowest unoccupied molecular orbital) from the HOMO (highest occupied molecular orbital) in the dye, and such an electron is, second, injected to the conduction band of the semiconductor. Third, such an injected electron moves through the semiconductor network to the external circuit, fourth, the hole created after the excitation at the HOMO of the dye is recovered by an electron from the redox electrolyte. For working as solar cells in this system, it is important that the position of the LUMO is higher than the conduction band of the semiconductor and

the position of the HOMO is lower than the position of the redox potential of the electrolyte [14].

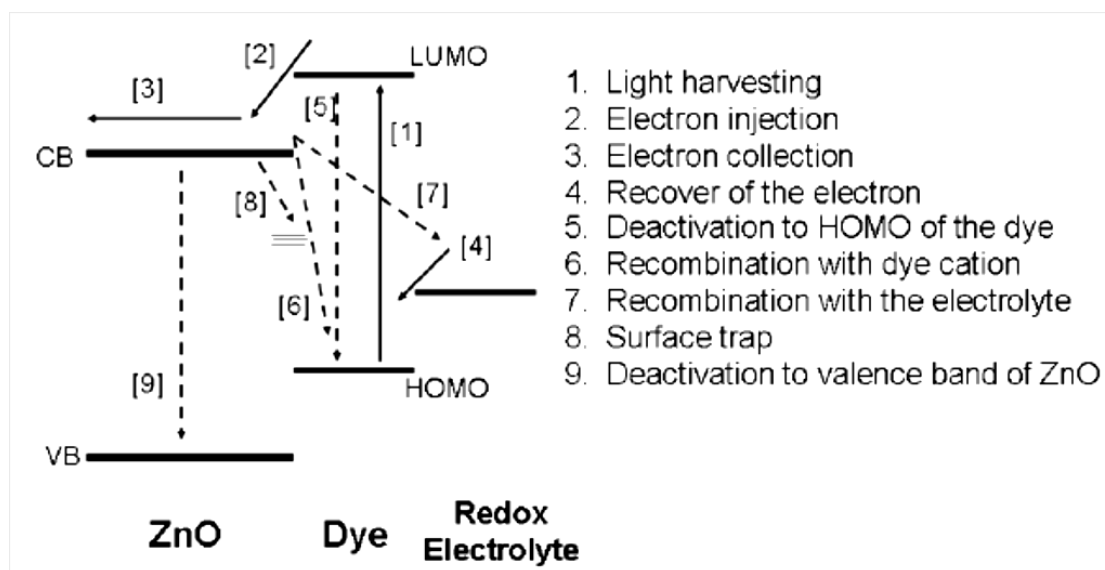


Figure 2.3 Model of the electron transport and the recombination process in dye-sensitized solar cells. Ideal electron transfers are indicated in solid line and undesirable electron transfers are indicated in dashed line [14].

In Figure 2.3, ideal and undesirable processes are shown. In the ideal case, an electron in a dye- modified metal oxide semiconductor electrode is collected at the external circuit without any disturbance. For such electron transfer, the electrode should fill the conditions of a good transport property in the semiconductor matrix (high electron collection efficiency) ([3] in Figure 2.3), a fast recovery of the electron to the oxidized dye (an electron supply from the redox electrolyte) ([4] in Figure 2.3) and a good electron separation (charge injection from the sensitizer to the semiconductor) ([2] in Figure 2.3). Normally, the transportation of the electron through the semiconductor matrix is milli, micro second range. The injection of electrons occurs on the picoseconds time scale. And the reduction of the dye cation by

$I^-$  in the electrolyte occurs in a few to tens of microseconds, depending on the concentration and species of cations. The injection yield depends on the particle size and crystallinity of the metal oxide semiconductor and the species and the concentration of the cations in the electrolyte. The recovery of the electron at HOMO of the dye from redox electrolyte occurs in 10 ns range. So it can be seen that overall process is limited by the electron transport in the semiconductor. Such gap of the times, however, gives a chance for the electrons to recombine before they reach the external circuit. An injected electron might recombine with the redox electrolyte, the oxidized dye, traps in the semiconductor or the valence band of the semiconductor. The recombination with the oxidized dyes takes tens of nanoseconds to a millisecond, depending on the density of electrons in the metal oxide semiconductor. And the recombination with the redox electrolyte occurs in about 10 ms at a light intensity corresponding to illumination of the earth surface by the sun (conditions often referred to as “1 sun”). This recombination process is almost negligible under short circuit conditions where the average transit time for the collection of electrons is shorter than the characteristic time constant for the back reaction. To confirm such slow back reactions, the electron lifetime has been measured by various groups, showing that the lifetime scales between a few milliseconds to more than one second. The photovoltage of dye- sensitized solar cells can at most reach the difference of the energy between the conduction band of the semiconductor and the redox potential of the electrolyte. The photovoltage of real electrodes is less than this maximum value because the position of the Fermi level and the increased back reaction at an open circuit condition decreases the photovoltage. Many researchers are studying intensively to enhance the photovoltage [14].

### **2.1.3 Materials of the dye-sensitized solar cell**

The components of the state-of-the-art dye-sensitized solar cell have changed relatively little since its inventing over ten years ago. The development has concentrated on the one hand to the tuning of the properties of the original components, such as the morphology and surface properties of the TiO<sub>2</sub> electrode and the chemical composition of the electrolyte. On the other hand new alternative materials and methods such as solid electrolytes and plastic substrates have been explored.

#### **1.) Substrates**

The electrodes of the standard DSSC are prepared onto transparent conducting oxide (TCO) coated glass substrates, between which the cell is assembled. The conducting coating of the substrate works as a current collector and the substrate material itself both as a support structure to the cell and as a sealing layer between the cell and the ambient air. Fluorine-doped tin oxide (SnO<sub>2</sub> : F) and indium tin oxide (In<sub>2</sub>O<sub>3</sub> : Sn or ITO) are the most frequently used TCOs in thin film photovoltaic cells. The standard preparation procedure of the nanostructured TiO<sub>2</sub> electrode includes sintering of the deposited TiO<sub>2</sub> film at 450-500 °C. As the only TCO coating stable at these temperatures, the SnO<sub>2</sub> : F has been the material of choice for DSSCs [15].

#### **2.) Metal oxide semiconductors**

Metal Oxide semiconductors are preferential in photoelectrochemistry because of their exceptional stability against photo-corrosion on optical excitation in the band gap [16]. Furthermore, the large band gap (>3 eV) of the oxide semiconductors is

needed in DSSCs for the transparency of the semiconductor electrode for the large part of the solar spectrum. In addition to  $\text{TiO}_2$ , semiconductors used in porous nanocrystalline electrodes in dye-sensitized solar cells include for example  $\text{ZnO}$ ,  $\text{CdSe}$ ,  $\text{CdS}$ ,  $\text{WO}_3$ ,  $\text{Fe}_2\text{O}_3$ ,  $\text{SnO}_2$ ,  $\text{Nb}_2\text{O}_5$ , and  $\text{Ta}_2\text{O}_5$ [17]. However, titanium dioxide has been, and still is, the cornerstone semiconductor for dye-sensitized nanostructured electrodes for DSSCs.

### 3.) Sensitizer dyes

As discussed above, the absorption of incident light in the DSSCs is realized by specifically engineered dye molecules placed on the semiconductor electrode surface. To achieve a high light-to-energy conversion efficiency in the DSSC, the properties of the dye molecule as attached to the semiconductor particle surface are essential. Such desirable properties can be summarized as [15]:

- Absorption: The dye should absorb light at wavelengths up to about 920 nanometers, i.e. the energy of the excited state of the molecule should be about 1.35 eV above the electronic ground state corresponding to the ideal band gap of a single band gap solar cell.
- Energetics: To minimize energy losses and to maximize the photovoltage, the excited state of the adsorbed dye molecule should be only slightly above the conduction band edge of the  $\text{TiO}_2$ , but yet above enough to present an energetic driving force for the electron injection process. For the same reason, the ground state of the molecule should be only slightly below the redox potential of the electrolyte.

- Kinetics: The process of electron injection from the excited state to the conduction band of the semiconductor should be fast enough to outrun competing unwanted relaxation and reaction pathways.
- Stability: The adsorbed dye molecule should be stable enough in the working environment (at the semiconductor-electrolyte interface) to sustain about 20 years of operation at exposure to natural daylight, i.e. at least  $10^8$  redox turnovers.
- Interfacial properties: good adsorption to the semiconductor surface
- Practical properties: e.g. high solubility to the solvent used in the dye impregnation.

Eosin yellowish (2',4',5',7'-tetrabromofluorescein, EY) is a well-known organic dye, characterized by a large  $\pi$  conjugated system, allowing  $\pi$ - $\pi^*$  transitions at low energy, i.e., in the visible part of the spectrum. Furthermore, this acidic molecule has an affinity for basic proteins and, in vivo, it gives different colors to the cells or to the tissues, according to the pH of the medium. For such peculiar characteristics EY has been widely used as a dye in many biological and medical fields, such as cytology, histology, hematology. In chemistry, it has been studied as a photocatalyst or as the main component in the fabrication of holographic optical elements, this latter application being related to its fluorescent properties [18].

More recently, eosin has attracted the attention of the electrochemists as one of the possible candidates as dye for application in molecular-based photovoltaic devices. In fact, in dye-based solar cells, the dye absorbs the light (i.e., the incoming photons) and an excited electron is then injected into the semiconductor conduction

band while the dye is regenerated in its native form by interaction with a redox pair (e.g.,  $\text{I}^-/\text{I}_3^-$ ) [18].

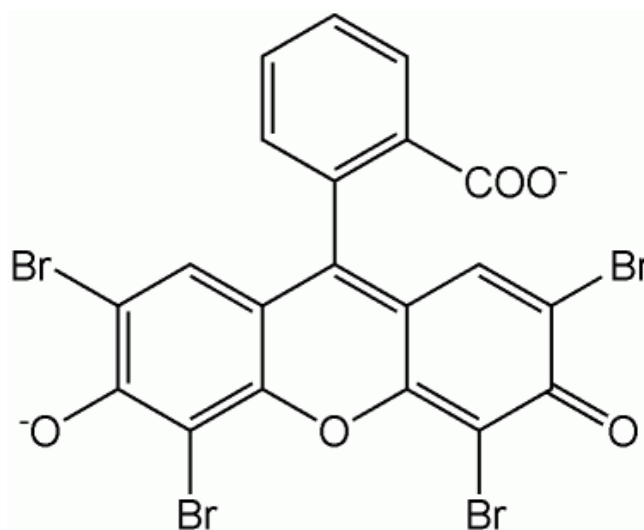


Figure 2.4 Structural formula of Eosin-Y [19].

Table 2.1 Properties of Eosin-Y dye.

<b>PROPERTIES [20]</b>	
<b>Molecular formula</b>	$\text{C}_{20}\text{H}_8\text{Br}_4\text{O}_5$
<b>Molar mass</b>	647.90 g/mol
<b>Classification</b>	fluorescent dyes
<b>Physical state</b>	orange to red powder
<b>Melting point</b>	295 °C
<b>Solubility in water</b>	freely soluble
<b>pH</b>	7-8

#### 4.) Electrolytes

The electrolyte used in the DSSCs consists of iodine ( $I^-$ ) and triiodide ( $I_3^-$ ) as a redox couple in a solvent with possibly other substances added to improve the properties of the electrolyte and the performance of the operating DSSC.

The ideal characteristics of the redox couple for the DSSC electrolyte [15]:

- Redox potential thermodynamically (energetically) favorable with respect to the redox potential of the dye to maximize cell voltage.
- High solubility to the solvent to ensure high concentration of charge carriers in the electrolyte.
- High diffusion coefficients in the used solvent to enable efficient mass transport.
- Absence of significant spectral characteristics in the visible region to prevent absorption of incident light in the electrolyte.
- High stability of both the reduced and oxidized forms of the couple to enable long operating life.
- Highly reversible couple to facilitate fast electron transfer kinetics.
- Chemically inert toward all other components in the DSSC.

Although DSSCs based on liquid electrolytes have reached efficiency as high over 11% under AM 1.5 ( $1000W/m^2$ ), the main problem is that the liquid electrolytes may limit device stability because the liquid may evaporate when the cell is imperfectly sealed, and more generally, permeation of water or oxygen molecules and their reaction with the electrolytes may worsen cell performance. Liquid electrolytes

also make the manufacture of multi-cell modules difficult because cells must be connected electrically yet separated chemically, preferably on a single substrate. Recently, many attempts have been made to solve the above problems by the replacement of liquid electrolyte with solid or quasi solid-state hole conductors [6].

### **5.) Counter-electrode catalysts**

For sufficiently fast reaction kinetics for the triiodide reduction reaction at the TCO coated cathode, a catalyst coating is needed.

As a traditional and usually most efficient catalyst, platinum has been used almost exclusively in the literature. However, the performance of the catalyst layer depends on the method by which the Pt is deposited onto the TCO surface. Platinum catalyst coating has been performed for example electrochemically, by sputtering, pyrolytically or by spin coating [15].

### **6.) Electrical contacts**

Similarly to the amorphous silicon and the other thin film solar cells deposited on TCO coated glass, the design of dye cells and modules is affected by the limited conductivity of the TCO layer. To keep the resistive losses in the TCO layer reasonably low, the longest distance from a photoactive point to a current collector should not exceed about 1 cm [21]. For example silver paint and adhesive copper tape can be used to extend the contact area of the current collector to fulfill this geometric requirement. In test cells alligator clips can be easily attached to these conductor strips.

A iodine based electrolyte is highly corrosive attacking most metals, such as silver, aluminum, copper, nickel and even gold, and can thus be particularly problematic when it comes to designing an electrical contacting of single cells in an integrated DSSC module [21].

## 7.) Sealing

Sealing the DSSCs has long been a difficult question because of the corrosive and volatile liquid iodide electrolyte used in the cells. Being directly related to the longterm stability of the cells it seems to be one of the main technological challenges of the DSSC technology [22]. A suitable sealing material should at least

- Be leak-proof to the electrolyte components and impermeable to both ambient oxygen and water vapor,
- Be chemically inert towards the electrolyte and other cell components, and
- Adhere well to the glass substrate and TCO coating.

Several sealing materials have been used, such as epoxy, water glass (sodium silicate), an ionomer resin Surlyn® (grade 1702) from Du Pont, aluminum foil laminated with polymer foil, a vacuum sealant Torr Seal, or a combination of these. Especially for research purposes sealing techniques based on O-rings and glass soldering have been developed.

### 2.1.4 Performance of the dye-sensitized solar cells

The performance of a solar cell is quantified on macroscopic level with parameters such as open-circuit voltage  $V_{oc}$ , short-circuit current  $J_{sc}$ , energy conversion efficiency  $\eta$ , and fill factor “ $FF$ ”. The parameters such as ideality factor

“ $n$ ” whose value is between 1 and 2 for DSSC [111] and reverse saturation current  $J_o$  have also been estimated. The other two parameters are the series resistance  $R_s$  and shunt resistance  $R_{sh}$ . In a DSSC,  $R_s$  is mainly attributed to the bulk resistance of semiconductor oxide films, transparent conducting oxide electrode, metallic contacts, and electrolyte, while  $R_{sh}$  accounts for the leakage path across the dye/oxide interface, induced by defects in the bulk and at the surface of the oxide. These parameters are determined using the  $J$ - $V$  characteristics. The values of  $\eta$  and  $FF$  were evaluated using the following relations [23].

$$FF = \frac{(J_{\max} \times V_{\max})}{J_{sc} \times V_{oc}} \quad (2.1)$$

$$\eta = \frac{(J_{sc} \times V_{oc} \times FF)}{P_{in}} \quad (2.2)$$

where  $P_{in}$  is the incident light power and  $J_{\max}$  and  $V_{\max}$  are the photocurrent and photovoltage for maximum power output ( $P_{\max}$ ).  $R_{sh}$  was determined from the slope of the  $J$ - $V$  curve of the cell at  $J = J_{sc}$  ( $V = 0$ ) and the  $R_s$  and  $n$  were calculated from the analysis of single  $J$ - $V$  characteristics of the solar cell (constant illumination level method).

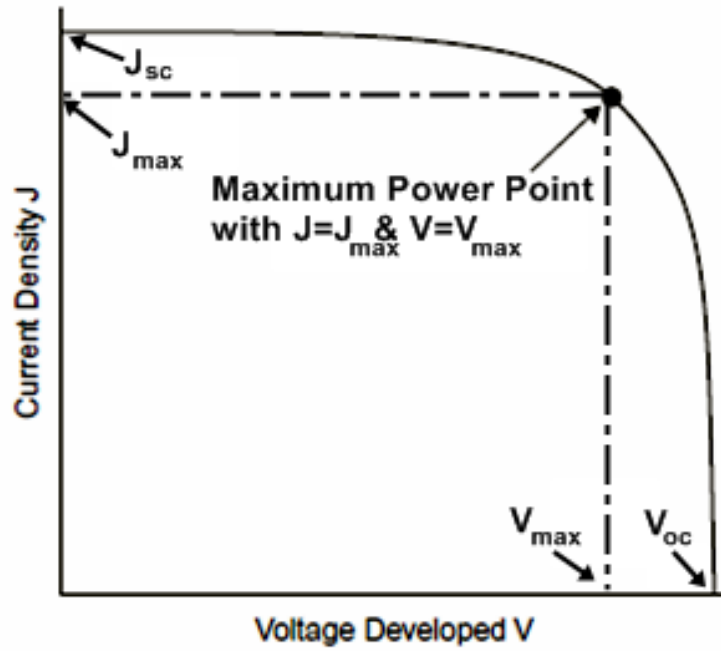


Figure 2.5 The current density-voltage ( $J$ - $V$ ) characteristic curve.

Knowing the values of  $R_s$ ,  $R_{sh}$ , and  $n$  the value of saturation current ( $J_o$ ) was determined as

$$J_o = \left( J_{sc} - \frac{V_{oc} - R_s J_{sc}}{R_{sh}} \right) \exp\left( -\frac{qV_{oc}}{nk_B T} \right) \quad (2.3)$$

Another important measurement in a DSSC is incident photon-to-current conversion efficiency (IPCE). In this measurement the efficiency is obtained at different wavelength of incident light. The IPCE of a cell is expressed in terms of the of the dye “LHE( $\lambda$ )”, the quantum yield of electron injection  $\eta_{inj}$ , and the efficiency of collecting the injected electrons  $\eta_{cc}$  at the back contact, i.e., IPCE ( $\lambda$ ) = LHE( $\lambda$ ) $\eta_{inj}\eta_{cc}$ . The IPCE has been calculated using the relation

$$\text{IPCE}(\%) = \frac{1240 \times j_{\text{sc}} (\text{mA} / \text{cm}^2)}{\lambda (\text{nm}) \times P_{\text{in}} (\text{mW} / \text{cm}^2)} \quad (2.4)$$

where  $J_{\text{sc}}$  is the short circuit current density,  $P_{\text{in}}$  is the light power density, and  $\lambda$  is the wavelength in nanometer.  $J_{\text{sc}}$  of the cells was determined from the  $J$ - $V$  characteristics of the cells obtained at different wavelengths of light using narrow bandwidth (10–12 nm) interference filters. The intensity of the incident monochromatic radiations was kept constant and measured using optical power meter.

### 2.1.5 Development of hole conductors in solid-state DSSCs

A schematic presentation of the structure of solid-state DSSCs is given in Figure 2.6. At the heart of the system is a mesoporous  $\text{TiO}_2$  film, which is placed in contact with a solid-state hole conductor. Attached to the surface of the nanocrystalline  $\text{TiO}_2$  film is a monolayer of a charge transfer dye. Photo-excitation of the dye results in the injection of an electron into the conduction band of the  $\text{TiO}_2$ . The original state of the dye is subsequently restored by electron donation from the hole conductor. The regeneration of the sensitizer by the hole conductor intercepts the recapture of the conduction band electron by the oxidized dye. The hole conductor is regenerated in turn at the counter-electrode, and the circuit is completed via electron migration through the external load [6].

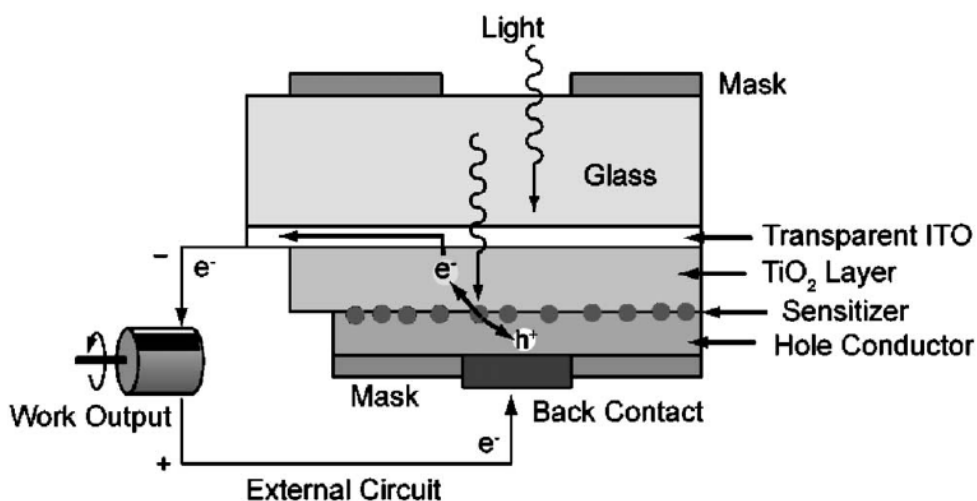


Figure 2.6 Structure of solid-state dye-sensitized nanocrystalline TiO<sub>2</sub> solar cells [6].

The hole conductors employed in solid-state DSSCs can be classified as p-type semiconductors, ionic liquid electrolytes and polymer electrolytes.

### 1.) P-type semiconductors [6]

Many inorganic p-type semiconductors satisfy several of the above requirements; however, the familiar large-band gap p-type semiconductors such as SiC and GaN are not suitable for use in DSSCs since the high-temperature deposition techniques for these materials will certainly degrade the dye. After extensive experimentation, a type of inorganic p-type semiconductor based on copper compounds such as CuI, CuBr, or CuSCN was found to meet all of these requirements.

These copper-based materials can be cast from solution or vacuum deposition to form a complete hole-transporting layer, and CuI and CuSCN share good conductivity in excess of  $10^{-2}$  S/cm, which facilitates their hole conducting ability.

A solid-state DSSC based on CuI was first demonstrated by Tennakone et al. [24] in 1995. The short-circuit current density was about 1.5–2.0 mA/cm<sup>2</sup> in sunlight (about 800 W/m<sup>2</sup>), which was probably the highest record for solid-state DSSCs up to then. By replacing cyanidin with a Ru-bipyridyl complex, Tennakone et al. reported an efficiency of 2.4% in solid-state DSSCs made with CuI.

One alternative to using CuI is employing CuSCN, which does not decompose to SCN<sup>-</sup> and there is no indication that stoichiometrically excessive SCN<sup>-</sup> creates surface traps in CuSCN. This is consistent with the observation that solid-state DSSCs based on CuSCN have more stable performance [25].

Compared with inorganic p-type semiconductors, organic p-type semiconductors (i.e. organic hole-transport materials) possess the advantages of having plentiful sources, easy film formation and low cost. Such organic materials have been widely used in organic solar cells, organic thin film transistors, and organic light-emitting diodes. In 1998, Grätzel et al [26], reported the first efficient solid-state DSSC employing amorphous organic hole-transport material (HTM), 2,2',7,7'-tetrakis (N,N-di-p-methoxyphenyl-amine)9,9'-spirobifluorene (OMeTAD) (Figure 2.7). By utilizing N(PhBr)<sub>3</sub>SbCl<sub>6</sub> and Li[(CF<sub>3</sub>SO<sub>2</sub>)<sub>2</sub>N] as the dopants, a maximum value of the incident monochromatic photo-to-current conversion efficiency (IPCE) of 33% and overall efficiency of 0.74% were obtained.

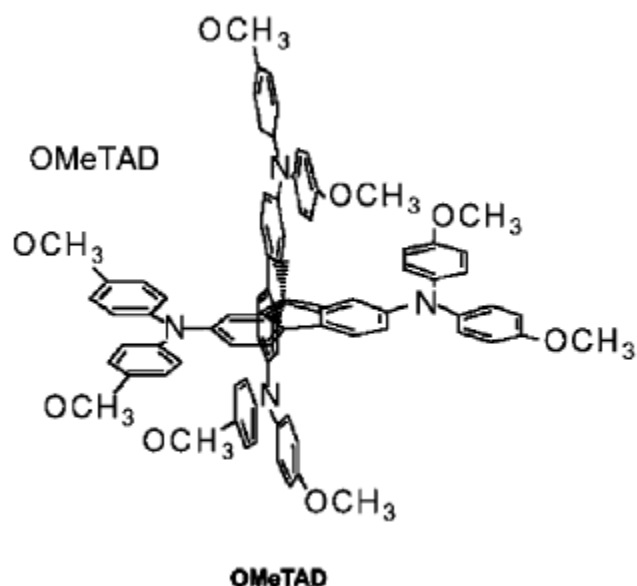


Figure 2.7 Organic p-type semiconductors utilized in solid-state DSSCs [5].

## 2.) Ionic liquid electrolytes

Room-temperature ionic liquids (RTILs) have good chemical and thermal stability, nonvolatility, negligible vapor pressure, nonflammability, and high ionic conductivity. When incorporated into DSSCs, they can be both the source of iodide and the solvent themselves.

Due to their nonvolatility, RTIL-based electrolytes have been applied to a 100 mm x 100 mm-sized DSSC[27]. For the purpose of fabricating such a large-sized DSSC, the influence of electrode distance, TiO<sub>2</sub> nano-particle size, and then thickness of the TiO<sub>2</sub> nano-porous layer was investigated by Matsui et al. in ionic liquid with a 1-ethyl-3-ethylimidazolium bis(trifluoromethanesulfonyl) amide(EMIm-TFSA) electrolyte system. In the optimal conditions, an energy conversion efficiency of 4.5% was obtained using a 9mm x 5mm small sized cell. The energy conversion efficiency of a large sized cell was 2.7% in the ionic-liquid system.

### 3.) Polymer electrolytes

The efficiencies of solid-state DSSCs utilizing p-type semiconductors were found to be unsatisfactory compared with those using organic liquid-phase redox electrolytes and the RTIL-based DSSCs still have the disadvantage of being fluid, the polymer electrolytes have been taken into account recently. It is of great importance that polymer electrolytes have the advantages of relatively high ionic conductivity and easy solidification. The use of conducting polymers as electrolytes or electrode materials for the development of plastic-like electrochemical devices is an appealing concept that dates back to the late 1960s.

Using a gel network polymer electrolyte is the usual way to improve the contact between solid electrolytes and nanoporous  $\text{TiO}_2$  or metal oxide layers. Actually, quasi solid-state DSSCs containing physical gels have been reported to have almost the same performance as those containing liquid gel precursors, which remain in a liquid state before becoming gelled to a solid-state gel. The process for the fabrication of quasi solid-state DSSCs is given in Figure 2.8 [28]. Gel electrolyte precursors containing liquid electrolytes and gelators are injected into cells that are already set. Gelation is usually carried out in the cell by heating the cell. Gel electrolyte precursors are liquid at first, which makes it possible for the precursors to be impregnated into nanoscale pores of  $\text{TiO}_2$  or metal oxide films. By heating, gelators propagate along a three-dimensional polymer network in the cell. Several conditions are necessary for gel electrolytes [28]:

- Polymerization must occur in the presence of iodine.
- Polymerization must occur at a temperature below which the dye would not decompose.

- Polymerization should be able to be initiated and completed even in the presence of some impurities such as oxygen, water, ions and so on.
- Polymerization has to be completed without generating byproducts that could decrease the photovoltaic performance.
- Polymerization can proceed without an initiator because the resultant decomposition products of the initiator may decrease the photovoltaic performance.

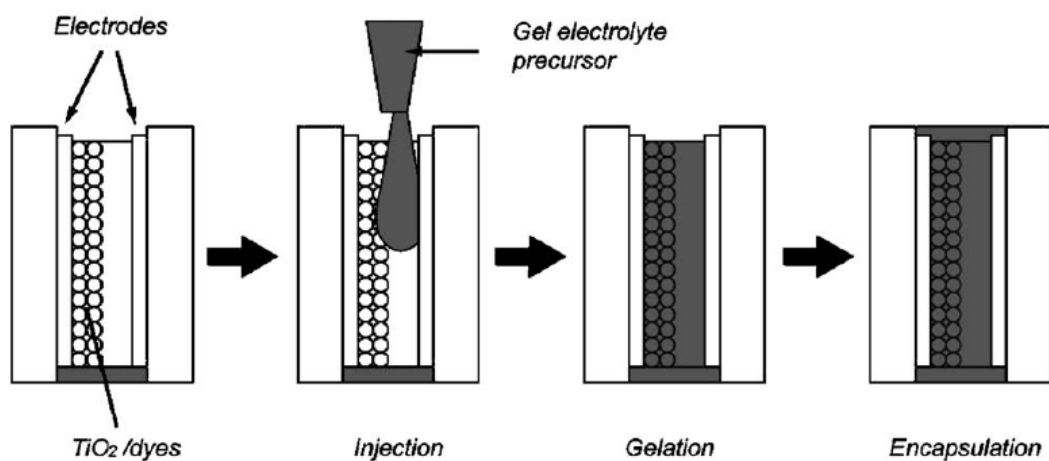


Figure 2.8 Process for fabrication of quasi solid-state DSSCs based on gel electrolyte

[28].

### 2.1.6 Literature review of quasi solid-state DSSCs based on polymer electrolyte

J. E. Benedetti et al. (2010) have prepared A polymer gel electrolyte composed of a poly(ethylene oxide) derivative, poly(ethylene oxide-co-2-(2-methoxyethoxy) ethyl glycidyl ether), mixed with gamma-butyrolactone (GBL), LiI and  $I_2$  is employed in dye sensitized solar cells (DSSC). The electrolyte is characterized by conductivity experiments, Raman spectroscopy and thermal analysis. The influence of the electrolyte composition on the kinetics of DSSC is also

investigated by transient absorption spectroscopy (TAS). The electrolyte containing 70 wt.% of GBL and 20 wt.% of LiI presents the highest conductivity ( $1.9 \times 10^{-3} \text{ Scm}^{-1}$ ). An efficiency of 4.4% is achieved using this composition. The increase in ISC as a function of GBL can be attributed an increase in the mobility of the iodide (polyiodide) species. The increase in the yield of the intermediate species,  $\text{I}_2^-$ , originating in the regeneration reaction, is confirmed by TAS [29].

S. Agarwala et al. (2011) have prepared A quasi-solid-state electrolyte employing a poly (ethylene oxide)/LiI system without a filler is evaluated. The electrolyte is optimized for various potassium iodide (KI) concentrations. The electrolyte containing 14.5 wt.% KI exhibits the highest conductivity ( $3.0 \times 10^{-3} \text{ Scm}^{-1}$ ). An efficiency of 4.5% is achieved using this composition of the electrolyte. It is shown that the introduction of KI in a conventional PEO/ $\text{I}_2$ /LiI electrolyte system prevents the crystallization of the polymer matrix and enhances the ionic conductivity. The energy conversion efficiency of the device is further enhanced to 5.8% by incorporating a lightscattering layer [30].

Z. Huo et al. (2007) have successfully prepared  $\text{TiO}_2$  nanoparticles was introduced into quasi-solid-state poly(vinylidene fluoride-co-hexafluoropropylene) (P(VDF-HFP)) based gel electrolyte to form nanocomposite gel electrolyte for quasi-solid-state dye-sensitized solar cells. The steady-state voltammograms revealed that the diffusion performance of the triiodide and iodide in the quasi-solid-state P(VDF-HFP) based gel electrolyte was greatly enhanced after the addition of  $\text{TiO}_2$  nanoparticles. By introducing  $\text{TiO}_2$  nanoparticles, the photoelectric conversion efficiency (AM 1.5) of the gel based device increased from 5.72% to 7.18%, which reached the level of the liquid electrolytes based device (7.01%). The results of the

accelerated aging tests showed that the nano-TiO<sub>2</sub> composite gel electrolytes based devices could maintain 90% of their initial value after heating at 60°C for 1000 h, which indicated that they had better thermostability than the corresponding normal gel electrolyte based devices and liquid electrolyte based devices [31].

K. -C. Huang et al. (2011) presented The effects of incorporation of aluminumnitride(AIN) in the gel polymer electrolyte (GPE) of aquasi-solid-state dye-sensitized solar cell (DSSC) were studied in terms of performance of the cell. The electrolyte, consisting of lithiumiodide (LiI) ,iodine(I<sub>2</sub>), and4-tert-butylpyridine (TBP) in3-methoxypropionitrile (MPN) ,was solidified with poly(vinyidene fluoride-co-hexafluoropropylene)(PVDF-HFP). The 0.05, 0.1, 0.3, and 0.5wt% of AIN were added to the electrolyte for this study. XRD analysis showed is duction of crystallinity in the polymer PVDF-HFP for all the additions of AIN. The DSSC fabricated with a GPE containing 0.1wt% AIN showed a short-circuit current density (JSC) and power-conversion efficiency ( $\eta$ ) of  $12.92 \pm 0.54$  mA/cm<sup>2</sup> and  $5.27 \pm 0.23\%$ , respectively, at 100mW/cm<sup>2</sup> illumination [32].

J.Y. Kim et al. (2008) presented to novel thixotropic gel electrolytes have been successfully prepared by utilizing oligomeric poly (ethylene oxide) (PEO)-based bis-imidazolium diiodide salts and hydrophilic silica nanoparticles for application in quasi-solid-state dye-sensitized solar cells (DSSCs). The thixotropic gel-state of the ionic liquid-based composite electrolytes is confirmed by observing the typical hysteresis loop and emporary hydrogen bonding. On using the PEO-based composite electrolyte, a quasi-solid-state DSSC exhibited highly improved properties such as easy penetration of the electrolyte into the cell without leakage, long-term stability,

high open-circuit voltage without the use of 4-tert-butylpyridine, and a high energy-conversion efficiency of 5.25% under AM 1.5 illumination ( $100\text{mWcm}^{-2}$ ) [33].

M. –S. Kang et al. (2008) reported the ternary component polymer-gel electrolytes are designed to facilitate ion transport in a highly viscous medium and utilize incident light more efficiently in dye-sensitized solar cells (DSSCs). Polyethers with multiple molecular size distributions are employed as solvents and TiO<sub>2</sub> nanoparticles as filler to prepare the polymer-gel electrolytes. The ion transport properties of the electrolytes are systematically investigated using electrochemical analyses such as ion conductivity and diffusion coefficient measurements. The influences of the electrolyte components on the electron transport in photoanodes are also investigated by measuring the laser-induced photovoltage and photocurrent transient response, incident photon-to-current efficiency (IPCE), and current–voltage ( $J$ – $V$ ) curves. The optimized polymer-gel electrolyte results in greatly enhanced energy conversion efficiency (*i.e.*, 7.2% at 1 sun) due to the significantly improved ion transport and good light-scattering effect of the nanofillers [34].

Z. Lan et al. (2007) presented a novel efficient absorbent for liquid electrolyte based on poly (acrylic acid) – poly (ethylene glycol) (PAA–PEG) hybrid is prepared. The highest value of liquid electrolyte absorbency about 3.65 is achieved. The polymer gel electrolyte shows a moderate value of ionic conductivity about  $3.24\text{mScm}^{-1}$  and high chemical stability. Based on the polymer gel electrolyte, a quasi-solid-state dye-sensitized solar cell was fabricated and its overall energy conversion efficiency of 3.19% was obtained under irradiation of  $100\text{mWcm}^{-2}$  [35].

Y. –H Lai et al. (2009) have studied two kinds of gel-type dye-sensitized solar cells (DSSCs), composed of two types of electrolytes, were constructed and the

respective cell performance was evaluated in this study. One electrolyte, TEOS-Triton X-100 gel, was based on a hybrid organic/inorganic gel electrolyte made by the sol-gel method and the other was based on poly (vinylidene fluoride-co-hexafluoro propylene) (PVDF-HFP) copolymer. TEOS-Triton X-100 gel was based on the reticulate structure of silica, formed by hydrolysis, and condensation of tetraethoxysilane (TEOS), while its organic subphase was a mixture of surfactant (Triton X-100) and ionic liquid electrolytes. Both DSSC gel-type electrolytes were composed of iodine, 1-propyl-3-methyl-imidazolium iodide, and 3-methoxy propionitrile to create the redox couple of  $I_3^-/I^-$ . Based on the results obtained from the  $I-V$  characteristics, it was found that the optimal iodine concentrations for the TEOS-Triton X-100 gel electrolyte and PVDF-HFP gel electrolyte are 0.05 M and 0.1 M, respectively. Although the increase in the iodine concentration could enhance the short-circuit current density ( $J_{sc}$ ), a further increase in the iodine concentration would reduce the  $J_{sc}$  due to increased dark current. Therefore, the concentration of  $I_2$  is a significant factor in determining the performance of DSSCs. In order to enhance cell performance, the addition of nanosilicate platelets (NSPs) in the above-mentioned gel electrolytes was investigated. By incorporating NSP-Triton X-100 into the electrolytes, the  $J_{sc}$  of the cells increased due to the decrease of diffusion resistance, while the open circuit voltage ( $V_{oc}$ ) remained almost the same. As the loading of the NSP-Triton X-100 in the TEOS-Triton X-100 gel electrolyte increased to 0.5 wt%, the  $J_{sc}$  and the conversion efficiency increased from 8.5 to 12 mA/cm<sup>2</sup> and from 3.6% to 4.7%, respectively [36].

## 2.2 Direct apply electron heating system

In this work used welding power supply in direct apply current heating due to welding usually requires high current which support in heating with materials.

### 2.2.1 Electric arc welding [37]

Welding is a fabrication or sculptural process that joins materials, usually metals or thermoplastics, by causing coalescence. This is often done by melting the workpieces and adding a filler material to form a pool of molten material (the *weld pool*) that cools to become a strong joint, with pressure sometimes used in conjunction with heat, or by itself, to produce the weld. This is in contrast with soldering and brazing, which involve melting a lower-melting-point material between the workpieces to form a bond between them, without melting the workpieces.



Figure 2.9 Gas metal arcs welding.

Many different energy sources can be used for welding, including a gas flame, an electric arc, a laser, an electron beam, friction, and ultrasound. While often an industrial process, welding can be done in many different environments, including open air, under water and in outer space. Regardless of location, however, welding

remains dangerous, and precautions are taken to avoid burns, electric shock, eye damage, poisonous fumes, and overexposure to ultraviolet light.

### 2.2.2 Welding power supply [38]

A welding power supply is a device that provides an electric current to perform welding. Welding usually requires high current (over 80 amperes) and it can need above 12,000 amps in spot welding. Low current can also be used; welding two razor blades together at 5 amps with gas tungsten arc welding is a good example. A welding power supply can be as simple as a car battery and as sophisticated as a modern machine based on silicon controlled rectifier technology with additional logic to assist in the welding process.



Figure 2.10 Welding power supply.

To supply the electrical energy necessary for arc welding processes, a number of different power supplies can be used. The most common classification is constant current power supplies and constant voltage power supplies. In arc welding, the voltage is directly related to the length of the arc, and the current is related to the amount of heat input. Constant current power supplies are most often used for manual

welding processes such as gas tungsten arc welding and shielded metal arc welding, because they maintain a relatively constant current even as the voltage varies. This is important because in manual welding, it can be difficult to hold the electrode perfectly steady, and as a result, the arc length and thus voltage tend to fluctuate. Constant voltage power supplies hold the voltage constant and vary the current, and as a result, are most often used for automated welding processes such as gas metal arc welding, flux cored arc welding, and submerged arc welding. In these processes, arc length is kept constant, since any fluctuation in the distance between the wire and the base material is quickly rectified by a large change in current. For example, if the wire and the base material get too close, the current will rapidly increase, which in turn causes the heat to increase and the tip of the wire to melt, returning it to its original separation distance.

The direction of current used in arc welding also plays an important role in welding. Consumable electrode processes such as shielded metal arc welding and gas metal arc welding generally use direct current, but the electrode can be charged either positively or negatively. In welding, the positively charged anode will have a greater heat concentration and, as a result, changing the polarity of the electrode has an impact on weld properties. If the electrode is positively charged, it will melt more quickly, increasing weld penetration and welding speed. Alternatively, a negatively charged electrode results in more shallow welds. Non-consumable electrode processes, such as gas tungsten arc welding, can use either type of direct current (DC), as well as alternating current (AC). With direct current however, because the electrode only creates the arc and does not provide filler material, a positively charged

electrode causes shallow welds, while a negatively charged electrode makes deeper welds.<sup>[14]</sup> Alternating current rapidly moves between these two, resulting in medium-penetration welds. One disadvantage of AC, the fact that the arc must be re-ignited after every zero crossing, has been addressed with the invention of special power units that produce a square wave pattern instead of the normal sine wave, eliminating low-voltage time after the zero crossings and minimizing the effects of the problem [39].

### **2.2.3 Literature review of direct apply electron heating process**

N. Abdenouri et al. (1999) presented that Transferred-arc plasma treatment of iron sulfides containing gold is examined from both thermodynamic and experimental points of view. Three cases are analyzed: argon plasma with sulfide, argon plasma with a carbon-sulfide mixture, and argonmethane plasma with sulfide. The carboreduction of the materials appears to be well adapted for gold separation by fuming, but experimentally the process is limited by the poor mixing of graphite with molten material. The reduction with a Ar-CH<sub>4</sub> (10%) plasma is a proved alternative to the aforementioned process. A gold extraction efficiency of 90% is achieved for batch smelting operations [40].

Y. Makino et al. (2003) have synthesized by using pulsed high current heating (PHC). In the method, the powder in a graphite die is pressed uniaxially and a pulsed direct current is applied. The pulsed direct current generates a spark discharge between particles. The crystallite size of the anatase densified using the PHC heating method gently increased from 10 nm (in the starting powder) up to 43 nm, with increasing relative density. While the size of the conventionally-densified anatase rapidly increased to over 50 nm irrespective of relative density [41].

P. Singjai et al. (2007) presented the Large-scale production for ZnO nanowires has been demonstrated by current heating deposition. Based on the use of a solid–vapor phase carbothermal sublimation technique, a ZnO–graphite mixed rod was placed between two copper bars and gradually heated by passing current through it under constant flowing of argon gas at atmospheric pressure. The product seen as white films deposited on the rod surface was separated for further characterizations. The results have shown mainly comb-like structures of ZnO nanowires in diameter ranging from 50 to 200 nm and length up to several tens micrometers. From optical testing, ionoluminescence spectra of as-grown and annealed samples have shown high green emission intensities centered at 510 nm. In contrast, the small UV peak centered at 390 nm was observed clearly in the as-grown sample which almost disappeared after the annealing treatment [42].

## **2.3 Copper sulfides**

### **2.3.1 Structure and properties [43]**

Copper sulfides describe a family of chemical compounds and minerals with the formula  $\text{Cu}_x\text{S}_y$ . Both minerals and synthetic materials comprise these compounds. Some copper sulfides are economically important ores.

Prominent copper sulfide minerals include  $\text{Cu}_2\text{S}$  (chalcocite) and  $\text{CuS}$  (covellite). In the mining industry, the minerals bornite or chalcopyrite, which consist of mixed copper-iron sulfides, are often referred to as “copper sulfides”. In chemistry, a “binary copper sulfide” is any binary chemical compound of the elements copper

and sulfur. Whatever their source, copper sulfides vary widely in composition with  $0.5 \leq \text{Cu/S} \leq 2$ , including numerous non-stoichiometric compounds.

The naturally occurring mineral binary compounds of copper and sulfur are listed below. There are probably more yet to be discovered, for example investigations of “blaubleibender covellite” (blue remaining covellite) formed by natural leaching of covellite (CuS) indicate that there are other metastable Cu-S phases still to be fully characterised.

- $\text{CuS}_2$ , villamaninite or  $(\text{Cu,Ni,Co,Fe})\text{S}_2$
- CuS, covellite
- $\text{Cu}_9\text{S}_8$  ( $\text{Cu}_{1.12}\text{S}$ ), yarrowite
- $\text{Cu}_{39}\text{S}_{28}$  ( $\text{Cu}_{1.39}\text{S}$ ) spionkopite
- $\text{Cu}_8\text{S}_5$  ( $\text{Cu}_{1.6}\text{S}$ ), geerite
- $\text{Cu}_7\text{S}_4$  ( $\text{Cu}_{1.75}\text{S}$ ), anilite
- $\text{Cu}_9\text{S}_5$  ( $\text{Cu}_{1.8}\text{S}$ ), digenite
- $\text{Cu}_{31}\text{S}_{16}$  ( $\text{Cu}_{1.96}\text{S}$ ), djurleite
- $\text{Cu}_2\text{S}$ , chalcocite

Table 2.2 Stable and some metastable copper sulfides [44]

Mineral or common name	Formulae used in the literature
<i>High-temperature phases</i>	
High-digenite	$\text{Cu}_2\text{S}$ , $\gamma\text{-Cu}_2\text{S}$ , $\alpha\text{-Cu}_2\text{S}$ , $\text{Cu}_{1.8}\text{S}$ , $\text{Cu}_{2-\delta}\text{S}$ , $\beta\text{-Cu}_{2-\delta}\text{S}$ , $\text{Cu}_{2-x}\text{S}$
High-chalcocite	$\text{Cu}_2\text{S}$ , $\beta\text{-Cu}_2\text{S}$ , $\beta\text{-Cu}_{2-\delta}\text{S}$
<i>Low-temperature phases</i>	
Low-chalcocite	$\text{Cu}_2\text{S}$ , $\alpha\text{-Cu}_2\text{S}$ , $\gamma\text{-Cu}_2\text{S}$ , $\text{Cu}_{2-\delta}\text{S}$
Djurleite	$\text{Cu}_{1.97}\text{S}$ , $\alpha\text{-Cu}_{1.97}\text{S}$ , $\text{Cu}_{1.96}\text{S}$ , $\text{Cu}_{1.95}\text{S}$ , $\text{Cu}_{1.94}\text{S}$ , $\text{Cu}_{1.938}\text{S}$ , $\text{Cu}_{31}\text{S}_{16}$
Anilite	$\text{Cu}_{1.75}\text{S}$ , $\text{Cu}_7\text{S}_4$
Covellite	$\text{CuS}$
<i>Metastable phases</i>	
Tetragonal phase	$\text{Cu}_{1.96}\text{S}$ , $\text{Cu}_{2-\delta}\text{S}_{\text{tet}}$
Low-digenite <sup>b</sup>	$\alpha\text{-Cu}_{2-\delta}\text{S}$ , $\text{Cu}_{1.8}\text{S}$ , $\text{Cu}_{1.81}\text{S}$ , $\text{Cu}_{7.2}\text{S}_4$ , $\text{Cu}_9\text{S}_5$ , $\text{Cu}_{9+x}\text{S}_5$ , $\text{Cu}_{9-x}\text{S}_5$ , $\text{Cu}_7\text{S}_4$
Roxbyite <sup>b</sup>	$\text{Cu}_{1.74-1.82}\text{S}$ , $\text{Cu}_7\text{S}_4$
Blue-remaining covellite, yarrowite	$\text{Cu}_{1.1}\text{S}$ , $\text{Cu}_9\text{S}_8$ , $\text{Cu}_{1+x}\text{S}$

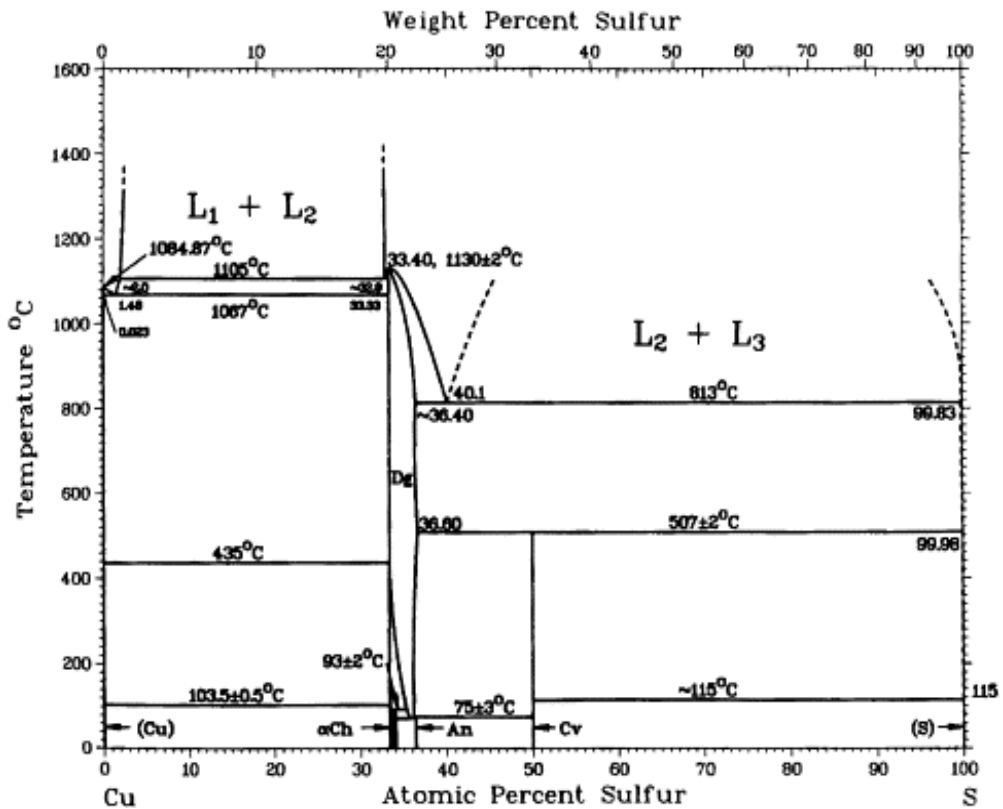


Figure 2.11 Copper sulfide phase diagram [44].

### 2.3.2 Classes of copper sulfides

#### 1.) Monosulfides

Their crystal structures consist of isolated sulfide anions that are closely related to either hcp or fcc lattices, without any direct S-S bonds. The copper ions are distributed in a complicated manner over interstitial sites with both trigonal as well as distorted tetrahedral coordination and are rather mobile. Therefore, this group of copper sulfides shows ionic conductivity at slightly elevated temperatures. In addition, the majority of its members are semiconductors [43].

Copper monosulfide (CuS) is a chemical compound of copper and sulfur. It occurs in nature as the dark indigo blue mineral covellite. It is a moderate conductor of electricity. A black colloidal precipitate of CuS is formed when hydrogen sulfide,  $H_2S$ , is bubbled through solutions of Cu (II) salts. It is one of a number of binary compounds of copper and sulfur and has attracted interest because of its potential uses in catalysis and photovoltaic [45].

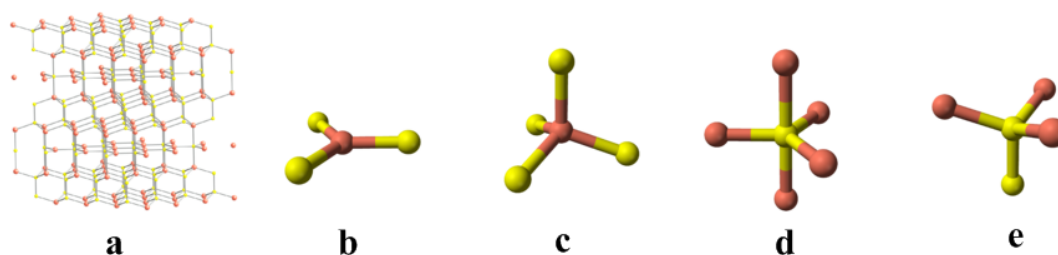


Figure 2.12 Crystal structures of CuS were explained each images (a-e) follow downstairs.

- a) Ball-and-stick model of part of the crystal structure of covellite.
- b) Trigonal planar coordination of copper .
- c) Tetrahedral coordination of copper ; 4 Cu atoms have tetrahedral coordination.
- d) Trigonal bipyramidal coordination of sulfur ; The 2 remaining S atoms form trigonal planar triangles around the copper atoms, and are surrounded by five Cu atoms in a pentagonal bipyramid.
- e) Tetrahedral coordination of sulfur-note disulfide unit.

Copper(I) sulfide is a copper sulfide, a chemical compound of copper and sulfur. It has the chemical compound  $\text{Cu}_2\text{S}$ . It is found in nature as the mineral chalcocite. It has a narrow range of stoichiometry ranging from  $\text{Cu}_{1.997}\text{S}$  to  $\text{Cu}_{2.000}\text{S}$ . There are two forms of  $\text{Cu}_2\text{S}$  a low temperature monoclinic form ("low-chalcocite") which has a complex structure with 96 copper atoms in the unit cell and a hexagonal form stable above  $104^\circ\text{C}$ . In this structure there are 24 crystallographically distinct Cu atoms and the structure has been described as approximating to a hexagonal close packed array of sulfur atoms with Cu atoms in planar 3 coordination. This structure was initially assigned an orthorhombic cell due to the twinning of the sample crystal.

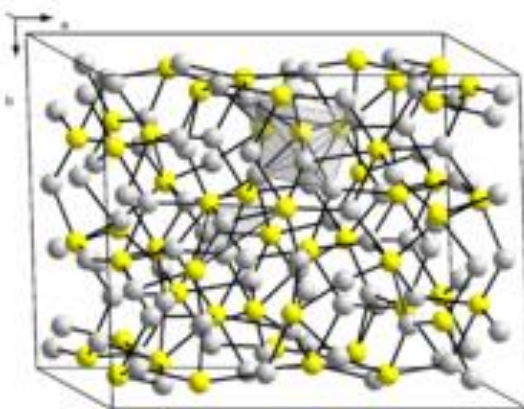


Figure 2.13 Crystal structure of  $\text{Cu}_2\text{S}$ [46].

## 2.) Mixed monosulfide and disulfide [47-50]

Compounds of copper contain both monosulfide ( $S^{2-}$ ) as well as disulfide ( $S_2$ )<sup>n-</sup> anions. Their crystal structures usually consist of alternating hexagonal layers of monosulfide and disulfide anions with Cu cations in trigonal and tetrahedral interstices. CuS, for example, can be written as  $Cu_3(S_2)S$ . Several nonstoichiometric compounds with Cu:S ratios between 1.0 and 1.4 also contain both monosulfide as well as disulfide ions. Depending on their composition, these copper sulfides are either semiconductors or metallic conductors. At very high pressures, a copper disulfide,  $CuS_2$ , can be synthesized. Its crystal structure is analogous to that of pyrite, with all sulfur atoms occurring as S-S units. Copper disulfide is a metallic conductor due to the incomplete occupancy of the sulfur p band.

Table 2.3 Copper sulfide identification.

Properties	Covellite	Chalcocite
Molecular formula	CuS	$Cu_2S$
Molar mass	95.611 g/mol	159.16 g/mol
Color	Indigo-blue or darker	Dark-gray to black
Mineralogy	Submetallic	Metallic
Density	4.6 g/cm <sup>3</sup>	5.6 g/cm <sup>3</sup>
Mohs scale hardness	1.5 - 2	2.5 - 3
Melting point	above 500 °C (decomposes)	1130 °C

Table 2.3 (continued)

Properties	Covellite	Chalcocite
Solubility	Soluble in HNO <sub>3</sub> , KCN, NH <sub>4</sub> OH, HCl, H <sub>2</sub> SO <sub>4</sub>	Slightly soluble in HCl; soluble in NH <sub>4</sub> OH; dissolves in KCN; decomposes in HNO <sub>3</sub> , H <sub>2</sub> SO <sub>4</sub>

### 2.3.3 Literature reviews of synthesis of copper sulfide

J. and Z. Zhang (2008) have been successfully prepared CuS in the presence of cation surfactant cetyltrimethylammonium bromide (CTAB) by hydrothermally treating the solution of CuCl<sub>2</sub>·2H<sub>2</sub>O and Na<sub>2</sub>S·9H<sub>2</sub>O at 180 °C for 24 h. The as-prepared CuS nanoplates are of hexagonal phase and are single crystal. The thickness and edge length of the nanoplates are about 15 nm and 60 nm, respectively. The experimental results have demonstrated a facile hydrothermal route to synthesize CuS nanoplates on a large scale. The uniform nanoplates are of hexagonal phase and are single crystal in nature. The PL spectrum indicated that the plate-like product had emission peak at 339 nm while the excitation wavelength was 230 nm. The UV–Vis spectrum shows that the absorption edge of the sample was about 630 nm and there was a significant red shift in CuS nanoplates [51].

F. Li et al. (2009) presented the controlled synthesis of copper sulfide (CuS) nanoplate-based architectures in different solvents has been realized at low cost by simply reaction of Cu(NO<sub>3</sub>)<sub>2</sub>·3H<sub>2</sub>O and S under solvothermal conditions without the use of any template. The products were all in hexagonal phase with high crystallinity and the morphology was significantly influenced by the solvents. The CuS products synthesized in dimethylformamide (DMF) were nanoplates and the samples prepared

in ethanol were flower-like morphology composed of large numbers of nanoplates, but those synthesized in ethylene glycol (EG) were CuS architectures with high symmetry made up of several nanoplates arranged in a certain mode [52].

T. Thongtem et al. (2007) were successfully synthesized CuS from copper and sulfur sources ( $\text{CuCl}_2 \cdot 2\text{H}_2\text{O}$ , CuBr,  $\text{Cu}(\text{CH}_3\text{COO})_2 \cdot \text{H}_2\text{O}$ ,  $\text{CH}_3\text{CSNH}_2$ ,  $\text{NH}_2\text{CSNHNH}_2$  and  $\text{NH}_2\text{CSNH}_2$ ) in ethylene glycol assisted by the cyclic irradiation of different microwave powers and prolonged times. By using XRD and SAED, CuS (hcp) was detected. The products characterized using SEM and TEM compose of assemblies of nano-flakes, clusters of nano-particles, nano-fibers, nano-rods and sponge-like structures influenced by the synthesized conditions. Their lattice vibrations are in the same Raman wavenumber at  $474 \text{ cm}^{-1}$ . Among the different products, the emission peaks are over the range 414-435 nm (2.85-2.99 eV) [53].

X. Wang et al. (2006) presented the one-step, solid-state reaction route was developed to synthesize copper sulfide (CuS) nanorods via grinding  $\text{Cu}(\text{NO}_3)_2 \cdot 3\text{H}_2\text{O}$  and  $\text{Na}_2\text{S} \cdot 9\text{H}_2\text{O}$  in existence of ethylenediamine tetraacetic acid disodium salt ( $\text{Na}_2\text{EDTA} \cdot 2\text{H}_2\text{O}$ ) at ambient temperature. The as-prepared CuS nanorods have diameters of 5 ~7 nm, lengths up to 40~70 nm. This method requires neither complex apparatus nor a long reaction time as usually needed in other methods [54].

J.G. Dunn and C. Muzenda (2001) presented the thermal oxidation of covellite of particle size 45-90  $\mu\text{m}$  was studied by heating 5-6 mg samples at  $20^\circ \text{C min}^{-1}$  in dry air in a simultaneous thermogravimetry-differential thermal analysis (TG-DTA) apparatus. By  $330^\circ\text{C}$ , a small amount of decomposition of covellite had occurred with the formation of cubic digenite ( $\text{Cu}_{1.8}\text{S}$ ). A mass loss was evident between 330 and  $422^\circ\text{C}$  associated with an exothermic peak. This event was assigned to the

decomposition of CuS to Cu<sub>2</sub>S followed by oxidation of the evolved sulfur. Between 422 and 474°C, an exothermic peak accompanied by a mass gain was observed [55].

H.T. Zhang et al.(2006) presented that trigonal and hexagonal CuS (covellite) nanoflakes with controlled size (10–200 nm, and thickness of 3.6–5 nm) were synthesized through the reaction between copper cetylacetate and sulfur in oleylamine. Size and shape of the products could be tuned by reaction parameters and reactant concentration. The as-prepared flakes have smooth surfaces and self-assemble face-to-face each other. This paper presents a novel procedure for the synthesis of CuS nanoflakes [56].

X.-H. Liao et al. (2003) presented the copper sulfide nanorods have been prepared by microwave irradiation of 1% (w/v) sodium dodecyl sulfate aqueous solution of copper nitrate and thioacetamide. Microwave power and reaction time have influenced on the formation of copper sulfide nanorods. The experiment showed that bumping would occur when the power was larger than 40%. When reaction time was less than 10 min the decomposition reaction was inadequate. The color of solution turned more and more deeply with increasing reaction time. When reaction time was over 15 min, the color of solution become dark, which shows the formation of copper sulfide [57].

S.-Y. Wang et al. (2003) presented that nanocrystalline Cu<sub>x</sub>S (x=1, 2) thin films were deposited by asynchronous-pulse ultrasonic spray pyrolysis (APUSP) technique on glass from CuCl<sub>2</sub> and thiourea at relatively low temperature without any complexing agent. The deposited films chemically close to CuS were found to be polycrystalline phases, while the Cu<sub>2</sub>S films were a mixture of amorphous and polycrystalline as well. The crystalline phase of particles was highly depended on the

molar ratio of thiourea to  $\text{CuCl}_2$  and the pyrolysis temperature. The growth of  $\text{Cu}_x\text{S}$  thin films was controlled successfully by the improved APUSP method. XRD and XPS analysis showed stoichiometric  $\text{Cu}_x\text{S}$  (covellite  $\text{CuS}$  and chalcocite  $\text{Cu}_2\text{S}$ ). Raman shifts of the films were measured at  $474\text{ cm}^{-1}$  ( $\text{CuS}$ ) and  $472\text{ cm}^{-1}$  ( $\text{Cu}_2\text{S}$ ) [58].

E. Godočíková et al. (2006) reported the thermal behaviour of mechanochemically synthesized nanocrystalline  $\text{CuS}$  particles by high-energy milling in an industrial mill has been studied. Structure properties were characterized by X-ray powder diffraction that reveals the formation of copper sulphide  $\text{CuS}$  as well as of copper sulphate  $\text{CuSO}_4 \cdot 5\text{H}_2\text{O}$ . Thermal properties of the as-prepared products were studied by the differential scanning calorimetry together with X-ray inspection for detection by pass products formed. The decomposition of the as-prepared sample has been studied too. Thermal stability of the anhydrous  $\text{CuSO}_4$  formed by the thermal decomposition is lower than the thermal stability of non-milled samples. The final product of the thermal decomposition is metallic copper instead of  $\text{Cu}_2\text{O}$ , which is stable up to  $1100\text{ }^\circ\text{C}$ . Differential scanning calorimetry (DSC) analysis proved that the percentage of chalcantite in the covellite mechanochemically synthesized by high-energy milling is 48–51% [59].

G. Mao et al. (2003) have investigated the making of copper sulfide nanorods using well-defined molecular templates. The films are characterized by AFM and XPS. The spin-coated monolayer of arachidic acid assembles on graphite as 1D nanostripes with bilayer periodicity. The copper arachidate film shows curved stripes, which become straight after reacting with hydrogen sulfide. The new template scheme may facilitate the fabrication of nanorod arrays of a variety of inorganic and semiconducting materials [60].

T. Thongtem et al. (2010) have presented covellite CuS hexaplates were successfully synthesized by the 200 °C solvothermal reactions of  $\text{CuCl}_2 \cdot 2\text{H}_2\text{O}$  and  $(\text{NH}_4)_2\text{S}$  in  $\text{C}_2\text{H}_5\text{OH}-\text{H}_2\text{O}$  mixed solvents containing HCOOH as a pH stabilizer, including different amounts and molecular weights (MWs) of polyethylene glycol (PEG). By using XRD and SAED, CuS (hcp) was detected. XRD peaks of the product, synthesized in a solution containing 5 g PEG6000 and 1.5 ml HCOOH for 5 h, are in accordance with those of the simulation and database. The (110) peak shows the preferential growth, corresponding to the hexaplates, characterized using SEM, TEM and HRTEM. CuS hexaplates with the (100) and (010) lattice planes at an angle of  $120^\circ$  were detected on the flat surface, and the (002) lattice plane on the edge. UV-vis absorption edge was detected at 610 nm (2.03 eV), and the PL emission at 361 nm (3.43 eV). Phase and morphology formations were also explained according to the experimental results [11].

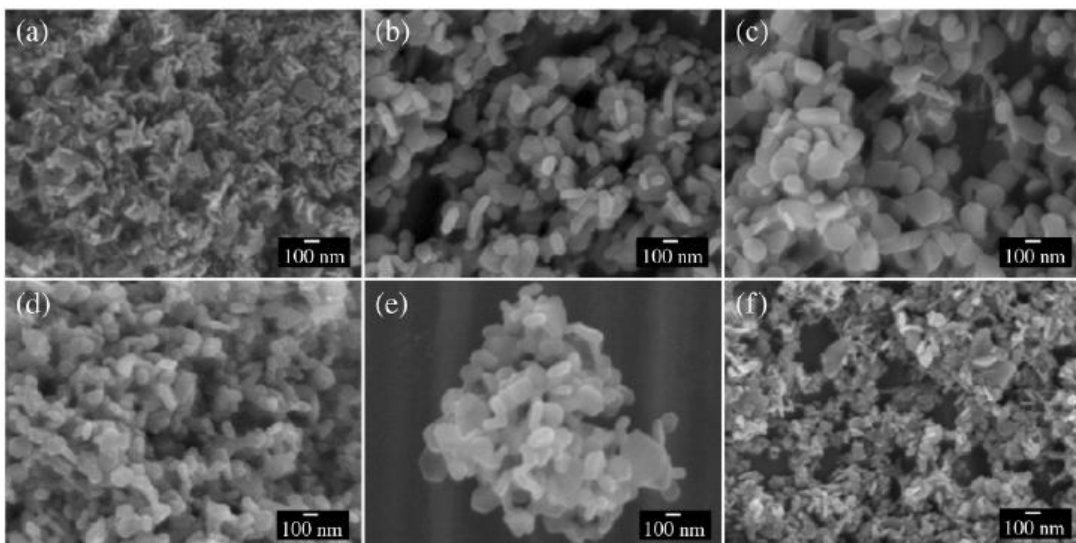


Figure 2.14 SEM images of the products in different conditions [11].

Y. Wu et al. (2008) presented the rational synthesis of colloidal copper(I) sulfide nanocrystals and demonstrate their application as an active light absorbing component in combination with CdS nanorods to make a solution-processed solar cell with 1.6% power conversion efficiency on both conventional glass substrates and flexible substrates with stability over a 4 month testing period [61].

L. Isac et al. (2010) have presented the films of  $\text{Cu}_x\text{S}$  with 217 -502 nm thickness were deposited by Automatic Spray Pyrolysis technique, at  $T = 275\text{-}325\text{ }^\circ\text{C}$ , from water:ethanol:glycerol= 7:2:1 (in volumes) solutions with molar ratio  $\text{Cu}:\text{S} = 1:2.5\text{-}3.5$ . Relative dense, homogenous and uniform films of  $\text{Cu}_x\text{S}$  ( $x = 1\text{-}2$ ), containing copper-rich phase digenite (single, predominant or secondary crystalline phase), with  $E_g = 2.41\text{-}3.1\text{ eV}$  and exhibiting electric resistance behavior were obtained. The optimized  $\text{Cu}_x\text{S}$  layers were integrated in 3D solar cells which show the diode behavior but the photovoltaic response is very low, in the experimental conditions [62].

## **2.4 Aluminium antimonide**

### **2.4.1 Structure and properties [63]**

Aluminium antimonide (AlSb) is a semiconductor of the group III-V family containing aluminium and antimony. The lattice constant is 0.61 nm. The indirect bandgap is approximately 1.6 eV at 300 K, whereas the direct band gap is 2.22 eV. Its electron mobility is  $200\text{ cm}^2\cdot\text{V}^{-1}\cdot\text{s}^{-1}$  and hole mobility  $400\text{ cm}^2\cdot\text{V}^{-1}\cdot\text{s}^{-1}$  at 300 K. Its refractive index is 3.3 at a wavelength of 2  $\mu\text{m}$ , and its dielectric constant is 10.9 at microwave frequencies. AlSb can be alloyed with other III-V materials to produce the

following ternary materials: AlInSb, AlGaSb and AlAsSb. However aluminum antimonide is rather flammable because of the reducing tendency of the antimonide ( $\text{Sb}^{3-}$ ) ion. It burns to produce aluminum oxide and antimony trioxide.

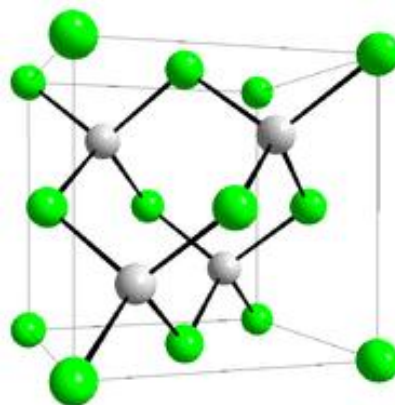


Figure 2.15 Crystal structure of AlSb

Table 2.4 Aluminium antimonide identification.

<b>Properties</b>	Aluminium antimonide
Molecular formula	AlSb
Molar mass	148.742 g/mol
Color	black crystals
Crystal system	Tetrahedral
Density	4.26 g/cm <sup>3</sup>
Melting point	1060 °C
Solubility in water	insoluble
Band gap	1.58 eV

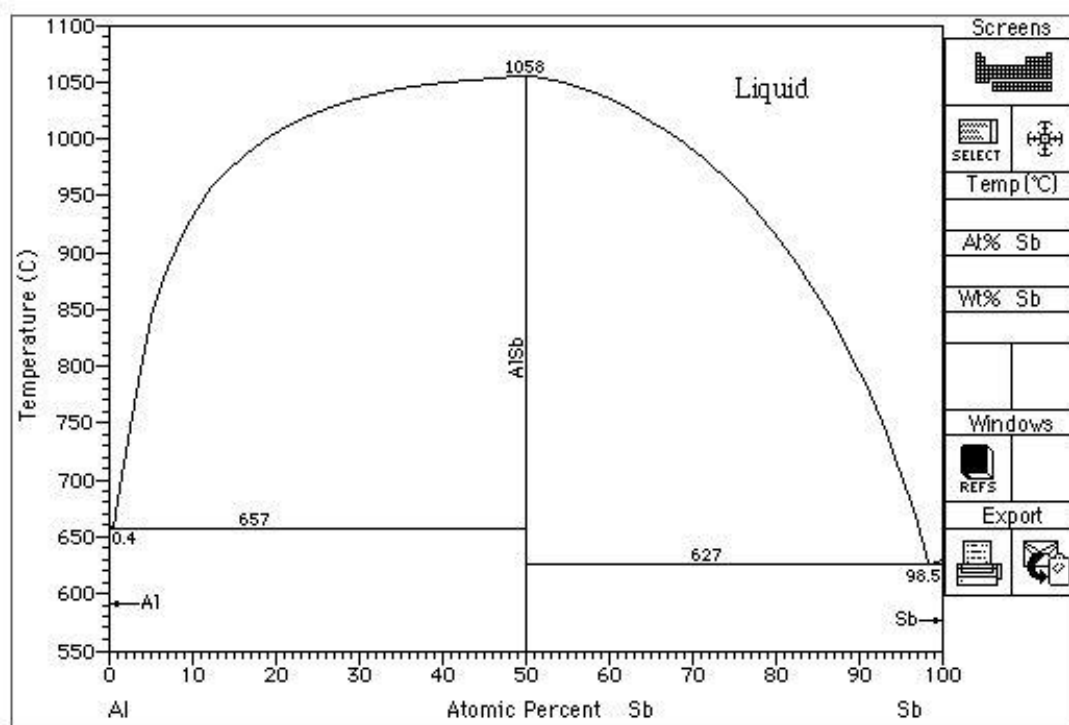


Figure 2.16 Aluminium antimonide phase diagram [64].

#### 2.4.2 Literature reviews of synthesis of aluminium antimonide

C.-M. Park and H.-J. Sohn (2008) presented a simple method of transforming micrometer-sized Al and Sb powders into a new nanocomposite modified with carbon by the alloying reaction of Al and Sb to form the AlSb phase and the dealloying reaction of the AlSb phase with carbon to synthesize the Sb/Al<sub>4</sub>C<sub>3</sub>/C nanocomposite was developed using a high-energy mechanical milling technique. The Sb/Al<sub>4</sub>C<sub>3</sub>/C nanocomposite was confirmed, using various analytical techniques, to be composed of a reduced crystalline Sb phase, amorphous Al<sub>4</sub>C<sub>3</sub> phase, and amorphous carbon. This novel nanocomposite showed a highly reversible reaction with Li, a high capacity of 687 mAh g<sup>-1</sup> with a good Coulombic efficiency of 85% for the first cycle, and high capacity retention above 520 mAh g<sup>-1</sup> over 200 cycles. Additionally, by controlling

the voltage window, an excellent cyclability with a high rate capability also was achieved. These excellent electrochemical properties demonstrated by the Sb/Al<sub>4</sub>C<sub>3</sub>/C nanocomposite electrode confirm its potential as a new alternative anode material for Li-ion batteries [65].

T. Gandhi et al. (2008) investigated a pulsed potential electrodeposition method using a room temperature molten salt system (aluminum trichloride, AlCl<sub>3</sub>/1-methyl-3-ethylimidazolium chloride, EMIC) with an addition of SbCl<sub>3</sub> is discussed. The potential pulse parameters were established by carrying out cyclic voltammetry at different concentrations of SbCl<sub>3</sub> and with varying molar ratios of AlCl<sub>3</sub>/EMIC. Stoichiometric AlSb deposits were obtained from an acidic AlCl<sub>3</sub>/EMIC (1.5:1 molar ratio) melt containing  $4 \times 10^{-3}$  mol/l of SbCl<sub>3</sub> onto an ordered TiO<sub>2</sub> nanotubular template. The AlSb compound was predominantly amorphous in as-deposited condition and annealing at 350 °C for 2 h in argon transformed into crystalline phase. The AlSb deposit showed a high resistivity in the order of  $10^9$  Ω-cm and a defect concentration of  $10^{16}$  cm<sup>-3</sup> which was attributed to presence of carbon. The deposits obtained from a basic melt (0.67:1 molar ratio of AlCl<sub>3</sub>/EMIC) were enriched with antimony [66].

H. Honda et al. (2003) have synthesized AlSb as an anode active material for lithium secondary battery using mechanical alloying (MA). Electrochemical performance was examined on the electrodes of AlSb synthesized with different MA time. The first charge (lithium-insertion) capacity of the AlSb electrodes decreased with increasing the MA time. The discharge capacity on repeating charge–discharge cycle, however, did not show the same dependence. The electrode, consisting of the 20 h MA sample exhibited the longest charge–discharge life cycle, suggesting that

there is the optimum degree of internal energy derived from the strain and/or the amorphization due to mechanical alloying. These results were evaluated using ex situ X-ray diffraction and differential scanning calorimetry[67].

G. Balakrishnan et al. (2005) have described the growth mechanisms of highly mismatched ( $\Delta a_o/a_o=13\%$ ) defect-free AlSb on Si(001) substrates. Nucleation occurs during the first few monolayers of AlSb deposition by crystalline quantum dot formation. With continued growth, the islands coalesce into a bulk material with no vertically propagating defects. Strain energy from the AlSb/Si interface is dissipated by crystallographic undulations in the zinc-blende lattice, as confirmed by high-resolution transmission electron microscopy (TEM) images. Reciprocal space analysis of the TEM images corroborates a crystallographic rotation associated with the undulations. The resulting AlSb material is >98% relaxed according to x-ray diffraction analysis [68].

R. Pino et al. (2006) have presented Bulk crystal growth of aluminum antimonide (AlSb) (50mm diameter) in silica crucibles without any sticking problem has been demonstrated for the first time. The adhesion of AlSb melt to silica crucible could be eliminated by employing a LiCl–KCl encapsulation in conjunction with excess antimony in the melt. This paper also presents a new surface preparation recipe based on KOH treatment that has been found to result in superior AlSb surfaces necessary for making reliable ohmic contacts for electrical property measurements [69].

C. L. Aravinda and W. Freyland (2006) have reported aluminium antimonide nanoclusters with an apparent band gap energy of  $0.92 \pm 0.2$  eV have been electrodeposited from the neutral ionic melt  $\text{AlCl}_3$ –1-butyl-3-methylimidazolium

chloride  $\{\text{AlCl}_3\text{-}[\text{C}_4\text{mim}]^+\text{Cl}^-\}$  at room temperature and have been characterized in-situ by electrochemical scanning tunneling microscopy (STM) and spectroscopy (STS) [70].

## 2.5 Plasma state

At atmospheric pressures and temperatures around 5000 K materials only exist in the gaseous phase. Above 10,000 K ions are the main constituent particles of matter. Under these conditions and at even higher temperatures, matter is considered to be in the plasma state. More elevated temperatures induce very high degrees of ionization, and temperatures of  $10^8$  K and higher lead to mixtures of bare nuclei and electrons. Sir William Crooks (1879) suggested the concept of the “fourth state of matter” for electrically discharged matter and Irving Langmuir first used the term “plasma” to denote the state of gases in discharge tubes [71].

### 2.5.1 Classification of plasmas

Plasma states can be divided in two main categories: Hot Plasmas (near-equilibrium plasmas) and Cold Plasmas (non-equilibrium plasmas). Hot plasmas are characterized by very high temperatures of electrons and heavy particles, both charged and neutral, and they are close to maximal degrees of ionization (100%). Cold plasmas are composed of low temperature particles (charged and neutral molecular and atomic species) and relatively high temperature electrons and they are associated with low degrees of ionization ( $10^{-4}$ –10%). Hot plasmas include electrical arcs, plasma jets of rocket engines, thermonuclear reaction generated plasmas, etc. while cold plasmas include low-pressure direct current (DC) and radio frequency (RF)

discharges (silent discharges), discharges from fluorescent (neon) illuminating tubes. Corona discharges are also identified as cold plasmas [71].

### 2.5.2 Low-pressure, non-equilibrium plasmas [71, 72]

Low-pressure non-equilibrium discharges (cold plasmas; below 1000 K) are initiated and sustained by DC, RF, or microwave (MW) power transferred to a low-pressure gas environment, with or without an additional electric or magnetic field. Ultimately, all these discharges are initiated and sustained through electron collision processes under the action of the specific electric or electromagnetic fields. Accelerated electrons (energetic electrons) induce ionization, excitation and molecular fragmentation processes leading to a complex mixture of active species, which will undergo, depending on the specific plasma mode (e.g. direct or remote plasma environments), recombination processes in the presence or absence of the plasma. The recombination reaction mechanisms are very different reaction mechanisms from those for conventional chemical processes [71]. To understand the influence of the frequency of electromagnetic fields, one has to study the energy transfer to charged particles in an oscillating electrical field. The energy  $U$  transferred to a particle with the electric charge  $Q$  in an electrical field with the frequency  $f$  is inversely proportional to the mass of the particle  $m$  and the squared frequency.

$$U \propto \frac{Q}{mf^2} \quad (2.5)$$

As the mass of the electrons is a few thousand times smaller than the mass of the ions, a few thousand-fold larger amount of energy is transferred to the electrons, as compared to the energy transferred to the ions. In addition, an RF system works with frequencies up to the megahertz range; microwave systems are in the gigahertz range. Therefore, in a microwave system, there is six orders of magnitude less energy transferred to the charged particles as compared to an RF system. This favors low-temperature systems. In both cases, the plasma is not in thermal equilibrium; the “temperature” of the electrons is significantly higher than that of the ions or neutral particles. The “reaction temperature” is therefore an average value determined at the exit of the plasma zone.

Equation (2.5) is valid for one isolated charged particle in an oscillating electrical field only. The situation is different in plasma, there; one finds free electrons, ions, dissociated gas and precursor molecules in addition to neutral gas species. Therefore, collisions between charged and uncharged particles limit the mean free path of the charged particles accelerated in the electric field. This influences the energy transfer to the particles. The collision frequency  $z$  of the gas species must therefore be considered. This changes equation (2.5) to:

$$U \propto \frac{Q}{mf^2} \left( \frac{z}{f^2 + z^2} \right) \quad (2.6)$$

Equation (2.6) shows the reduction of the energy transfer to the charged particles by collision with other neutral species. The collision frequency  $z$  in the plasma depends on the gas pressure. As a rule of thumb, one can say: In a RF system,  $z$  is significantly

larger than  $f$  ; whereas in microwave systems,  $z$  and  $f$  are almost equal, usually, the gas pressure is adjusted such that the microwave frequency is larger than the collision frequency. This makes a significant difference. In RF systems, because of the short free path length of the electrons, the energy of the electrons is in the range of a few eV, whereas the energy of electrons in a microwave plasma is in the range of keV.

### 2.5.3 Microwave plasma system

These plasmas are sustained by microwave energy dissipated into the reaction media by coaxial cables or by waveguides in the case of higher powers. The physical dimensions of coaxial cables (cross-sections) and waveguides are selected according to the microwave frequency. Vollath [73] succeeded as the first one to design such a system. It is shown in Figure 2 .18

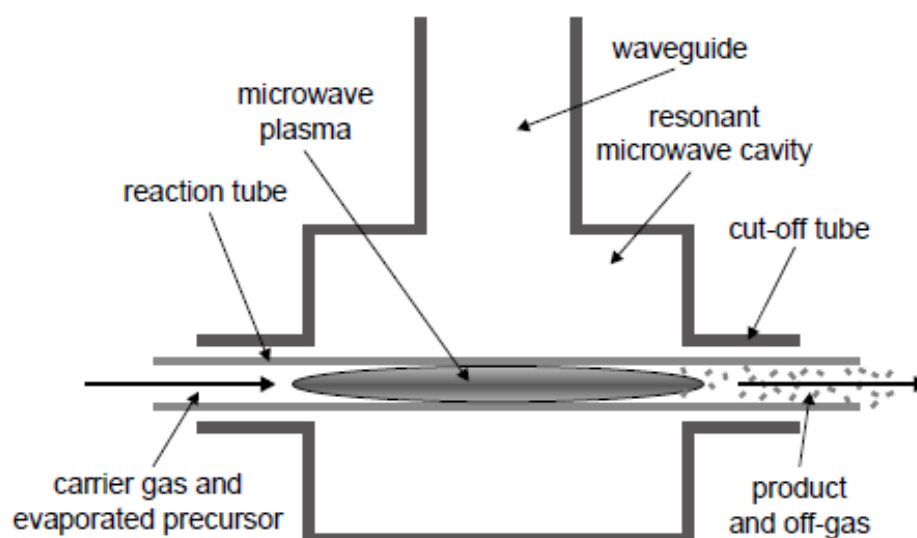


Figure 2.17 Design of a microwave plasma system working at reduced pressure. The cut-off tube, an important part of the microwave design, prevents microwaves leaking outside of the cavity.

Most of materials efficiently absorb or reflect microwaves, and as a result microwave energy cannot be transported using conventional cables. Microwave discharges are more difficult to sustain under low-pressure conditions (<1 Torr). In a collisionless condition the energy gained by an electron during one cycle is too small to produce ionization. In collisional plasmas at constant power density and electric field, the average (RF) microwave power transferred from the driving field has a maximum value when the collision frequency equals the driving frequency. The absorption of microwave power depends on the collision frequency of the electrons which is controlled by the atomic and molecular species. At comparable plasma parameters, RF discharges most often fill the entire reactor, whose dimensions are usually smaller than the wavelength of the RF field (13.56 MHz corresponds roughly to 22 m). Microwave plasmas exhibit a strong peaking in field intensity at the coupling to the microwave cavity that diminishes gradually with increased distance from the coupling owing to the energy originating at the microwave coupling, rather than being deposited throughout the discharge. ( $\lambda=12.24$  cm at 2.54 GHz).

Electrons with energies of just a few eV can attach to the surface of particles; this is different in the case of energy rich electrons, as they ionize the particles. Therefore, in RF systems, one expects negatively charged particles, whereas the electric charge of particles in microwave systems is positive. In both cases, in good approximation, the electric charge of the particles increases linearly with the particle diameter [72].

Figure 2.17 shows the charge of nanoparticles in an RF electrical field as a function of the diameter. The increasing charging of the particles with increasing diameter has severe consequences on the processes of particle coagulation and

agglomeration. Particles with electric charges of equal sign repel each other. As the charge of the particles increases with increasing particle diameter, particles with larger diameters repel each other more than ones with smaller diameters. This suppresses the formation of larger particles and the formation of agglomerates.

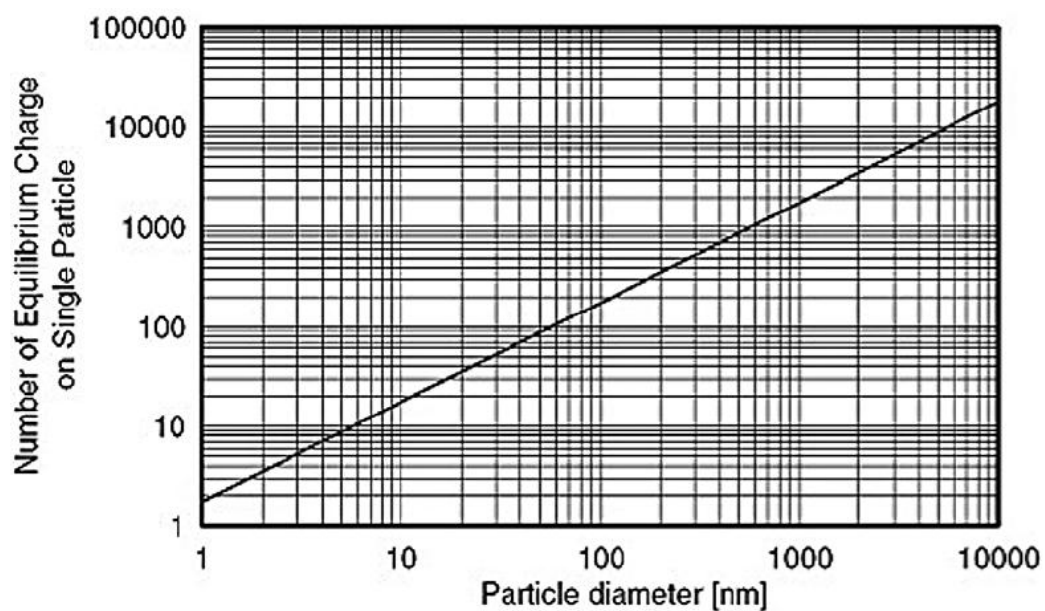


Figure 2.18 Average numbers of electric charges carried by a single nanoparticle. The particle charge increases linearly with the diameter over many orders of magnitude which reproduced by permission of Springer.

In other words: In a well-designed low-temperature plasma system for the synthesis of nanoparticles, one obtains particles with a narrow particle size spectrum [72].

#### 2.5.4 Literature review of synthesis by microwave plasma

A. Irzh et al. (2010) have represented a new method to synthesis of ZnO and/or Zn nanoparticles by means of microwave plasma (Figure 2.19, 2.20) whose electrons are the reducing agents. Glass quadratic slides sized  $2.5 \times 2.5$  cm were coated by ZnO and/or Zn particles whose sizes ranged from a few micrometers to 20 nm. The size of the particles can be controlled by the type of the precursor and its concentration. In the current paper, the mechanism of the reactions of ZnO and/or Zn formation was proposed. Longer plasma irradiation and lower precursor concentration favor the fabrication of metallic Zn nanoparticles. The nature of the precursor's ion (acetate, nitrate, or chloride) is also of importance in determining the composition of the product. The glass slides coated by ZnO and/or Zn nanoparticles were characterized by HR-SEM, HR-TEM, AFM, XRD, ESR, contact angle and diffuse reflectance spectroscopy (DRS) [74].

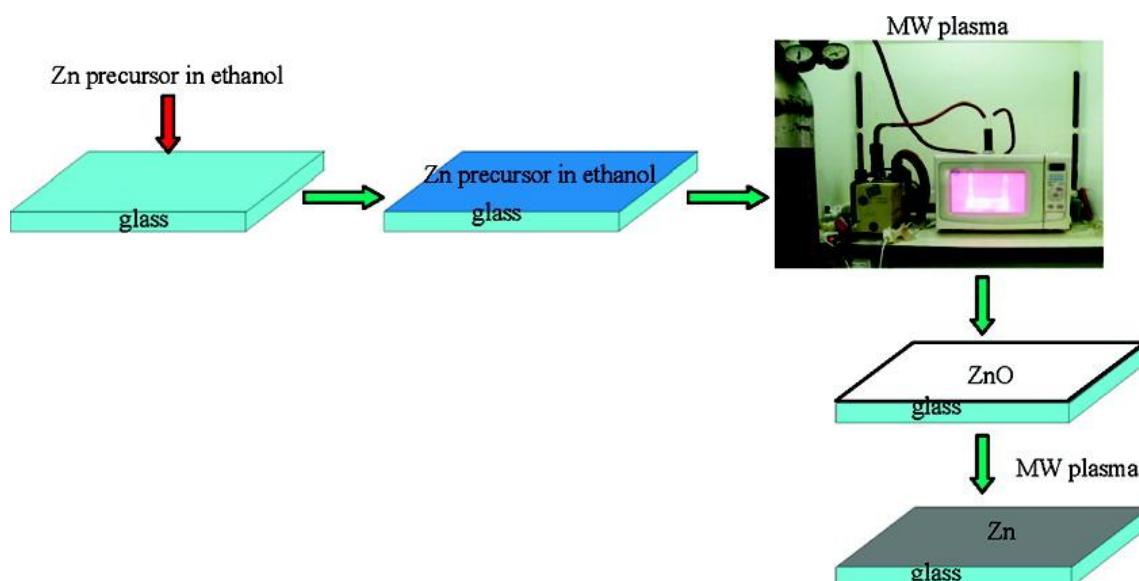


Figure 2.19 Schematic illustration of the procedure.

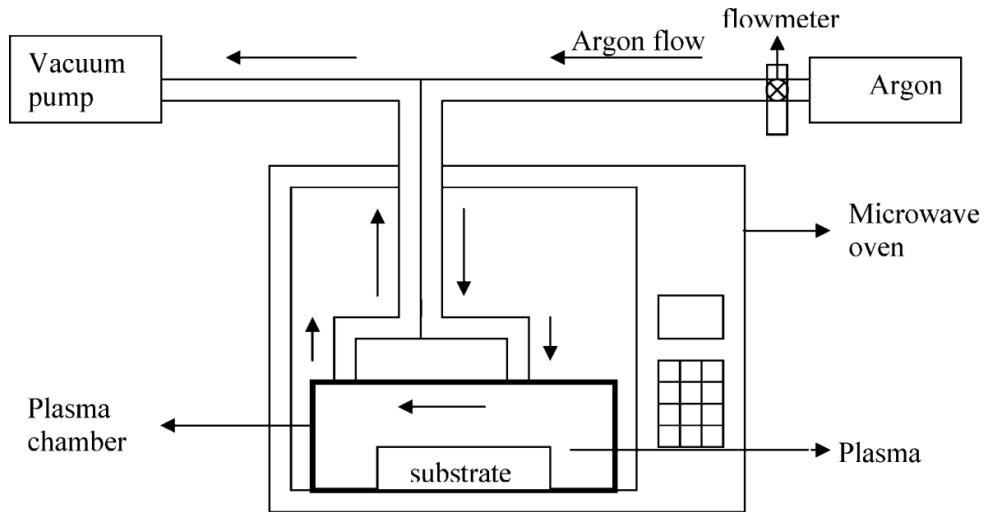


Figure 2.20 Schematic diagram of the reaction system.

Y. R. –Lazcano et al. (2009) have presented the copper sulfide thin films were grown by chemical deposition and post treated in air plasma during 20 min. Air plasma was generated by alternating current discharge at a pressure of  $4 \times 10^2$  Pa. The power discharge was maintained at an output of 220 V and a current of 0.2 A. Thermal annealing at 300 °C was performed for comparison. X-ray diffraction shows that plasma treatment results in phase transformation of  $\text{Cu}_{39}\text{S}_{28}$  (as grown) to CuS (treated by plasma). The copper lost is confirmed by X-ray fluorescence. No significant change in the optical band gap was observed due to plasma action. In addition, the electrical conductivity increases in one order of magnitude [75].

Q. Zhen et al. (2007) have been synthesized the high density nanocrystalline  $\text{Bi}_2\text{O}_3\text{-HfO}_2\text{-Y}_2\text{O}_3$  composite solid electrolyte by microwave plasma (Figure 2.21). After the samples were sintered in microwave plasma at 700 °C for 30 min, the relative density was found to be greater than 96%. Moreover, the sintered specimens exhibit considerably finer microstructure and greater densification compared to that of samples sintered by conventional pressureless sintering [76].

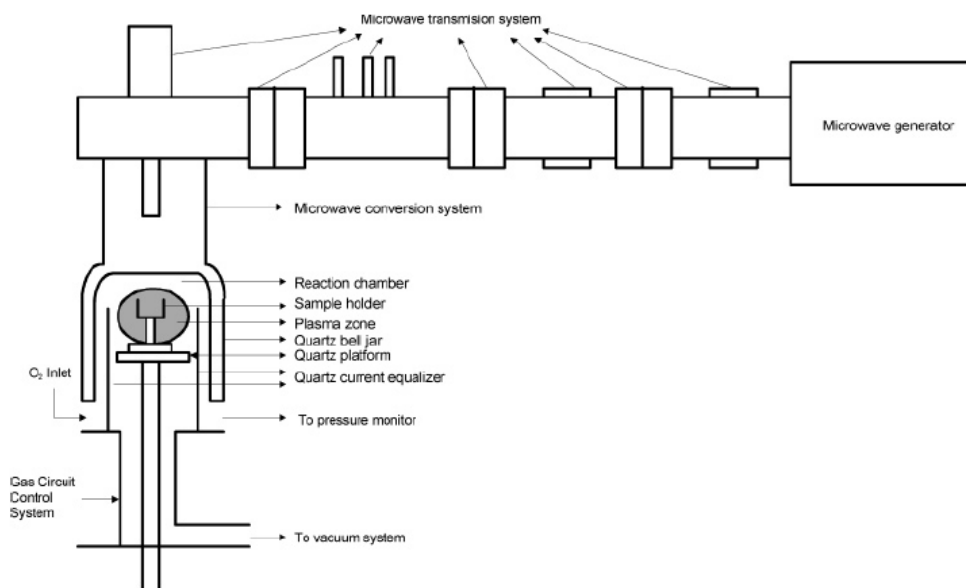


Figure 2.21 A schematic diagram of microwave plasma equipment.

J. D. Houmes and H. -C. Loyer (1997) presented the utility of microwave heating and microwave generated nitrogen plasmas as a synthetic technique toward the synthesis of nitrides is demonstrated. The synthesis of several binary and ternary nitrides, including TiN, AlN, VN, Li<sub>3</sub>FeN<sub>2</sub>, Li<sub>5</sub>TiN<sub>3</sub>, and Li<sub>3</sub>AlN<sub>2</sub>, using either a microwave heating source or a microwave generated nitrogen plasma (Figure 2.22), are described. Two types of reactions, those between a metal and a nitrogen plasma and those between Li<sub>3</sub>N and either a metal or a metal nitride in a microwave heating system are discussed [77].

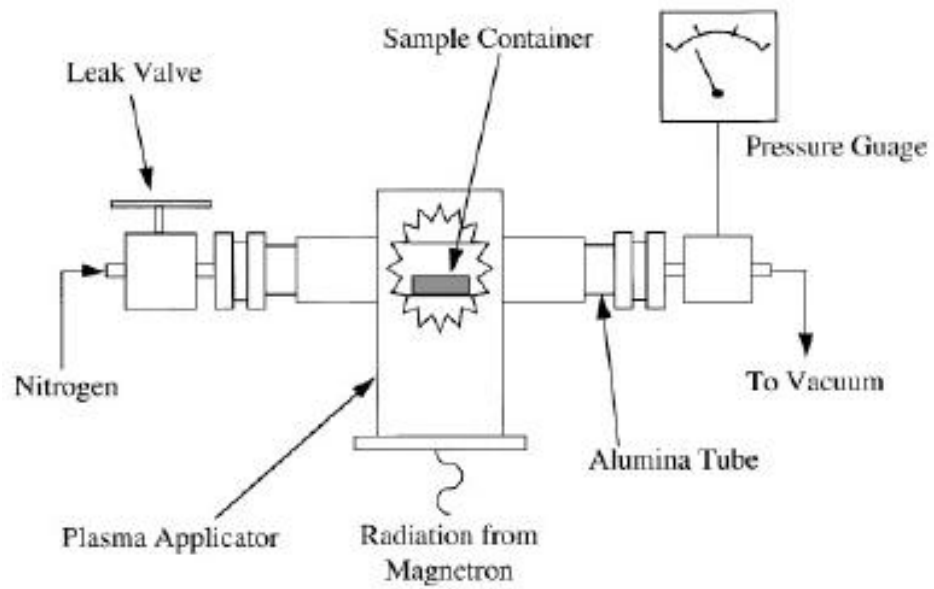


Figure 2.22 Schematic diagram of Cober microwave system used in the synthesis of binary nitride materials by reaction with a nitrogen plasma.